The following publication Sun, M., & Huang, B. (2020). A full picture of intrinsic defects induced self-activation of elastic potential fluctuation within monolayered metal chalcogenide. Nano Energy, 70, 104530. is available at https://doi.org/10.1016/j.nanoen.2020.104530.

A full picture of intrinsic defects in monolayer 2D ferroelectric materials

Mingzi Sun and Bolong Huang*

Department of Applied Biology and Chemical Technology, The Hong Kong Polytechnic University, Hung Hom, Kowloon, Hong Kong SAR, China

Email: bhuang@polyu.edu.hk

Abstract

Pursuing the precise structural identification of functional two-dimensional (2D) layered metal chalcogenides (LMCs) are key factors dominating the origins of the unique electronic and ferroelectric properties. However, the complicated phase change of In_2Se_3 and their high sensitivity towards the intrinsic defects still require the advanced technology to identify the origins of the inhomogeneous charge distribution induced in-plane and out-of-plane ferroelectricity. Herein, we have presented comprehensive theoretical research to reveal the simulated scanning tunneling microscope (STM) images as a toolbox for the experimental results to distinguish the structural features. Moreover, the corresponding electron-phonon behaviors of α-In_2Se_3 with major intrinsic defects provide pivotal references to explain the unique in-plane and out-of-plane electronic and ferroelectric properties in different applications, which is crucial for optimizing the growth of ultrathin 2D LMCs materials for future electronic devices.

Keywords: Defect activated charge coupling, mono-layered α-In_2Se_3, scanning tunneling microscope, density functional theory, ferroelectricity, layered metal chalcogenides

Introduction:

Following the developments of two-dimensional (2D) graphene with distinct properties, tremendous progress has been achieved for the broad applications of 2D materials in nanoscale electronics and optoelectronics [1-2]. To further compensate for the applications of graphene in ultrathin 2D electronics, the layered metal chalcogenides (LMC) contribute to a dominant group of the layered 2D structure with various properties and applications [3-8]. The LMCs consists of the metal with the chalcogen atom, which leads to over 40 different combinations [9]. These layered structures usually demonstrate the strong covalent bonds with the weak intra-layer van der Waals (vDW) interactions, endowing them with potential for future functional optoelectronic devices [10-11]. Recently, the finding of the ferroelectricity in the ultrathin film materials further increases the interest of scientists [12-14]. This offers an approach to new materials with new functionalities, in which LMC systems is becoming one of the focus [3, 15-19]. Meanwhile, the ferroelectric vdW material allows the nonvolatile switching and manipulation of both electrical and optical properties such as ferroelectric capacitors, ferroelectric tunnel junctions (FTJs), and ferroelectric field-effect transistors (FeFETs) [20-21]. The ultrathin 2D materials still meet the challenge of the loss of ferroelectricity, which is induced by several factors including the surface energy effect, depolarizing electrostatic field and electron screening. Ghosez and Junquera also confirmed that that the critical thickness challenge for ferroelectricity instability in perovskite ultrathin films, which is induced by a depolarizing electrostatic field from the dipoles at the ferroelectric–metal interfaces [22]. However, 2D LMCs systems usually exhibit several typical advantages such as scalability, low defect concentration, and perfect interface construction. 2D layered materials allow the self-limiting assembly, leading to the possible synthesis of varied scale size. The self-terminated atomic bonds within the 2D LMCs systems result in the superior capability of anti-oxidation with limited surface states.

Indium selenide (In_2Se_3) has become one of the most attractive LMC materials due to its flexible phases with broad applications in phase-change memory, lithium batteries, optoelectronic and even photovoltaic devices [23-26]. The different phases are In_2Se_3 depending on the synthesis approach and temperature control [27-29]. For both α and β phases, each layer possesses five covalently bonded monatomic sheets. Presently, α-In_2Se_3 are particularly attractive in the atomically thin film research due to the flexible phase modulations and unique electronic behaviors. Wang et al. have reported the coexistence of out-of-plane and in-plane piezoelectricity in the monolayer to bulk α-In_2Se_3, which breaks the limitation of piezoelectric polarization in ultrathin 2D LMCs with only the in-plane direction of odd-number layers [30]. The ferroelectricity within In_2Se_3 further promotes the focus of much research, requiring the careful identification of the lattice structure through the advanced technologies. Tao *et al.* have demonstrated the observation of reversible phase change of 2D In_2Se_3 by thermal excitation [31]. From the theoretical perspective, Ding *et al.* predicted the potential ferroelectricity in both in-plane and out-of-plane directions of In_2Se_3 [32]. Although the ferroelectricity in the ultra-thin 2D materials has been predicted, the related experimental works in the ultra-thin layer In_2Se_3 are very limited. Lai and co-workers firstly confirm the out-of-plane ferroelectricity by experiments [33]. Meanwhile, Zheng *et al.* have identified the in-plane ferroelectricity, which is strongly tied to the formation of one-dimensional superstructures in β'-In_2Se_3 [34]. Later, Li *et al.* have reported the interplay between the in-plane and out-of-plane ferroelectricity of the ultra-thin α-In_2Se_3 [35]. Previous reported works mostly focus on the out-of-plane ferroelectricity since the facile break of symmetry by the asymmetric position of the Se along the c-axis. However, all these works still focus on the several layered α-In_2Se_3 rather than the single-layer α-In_2Se_3, which is more sensitive to the polarization induced by the local defects.

The LMCs systems usually yield high responsivity to external excitation or environmental change due to large surface-to-volume ratio and the quantum confinement effects, which have been confirmed in α-In_2Se_3 as well [24, 36]. However, the synthesis of the monolayer or few layers of α-In_2Se_3 has been a challenge, which is only recently actualized by the exfoliation method or vapor deposition method [37-38]. It has been noted that α-In_2Se_3 demonstrates the thickness dependence of the electronic structure regarding the bandgap shift, which indicates the promising potential for realizing the flexible wavelength photo-detection [39]. Compared to the intense attention of the synthesis and characterization of α-In_2Se_3, a full picture of the interplay between defect and structural lattice is still lacking. The atomic scale insights into structure instability and defects supplied crucial references for future optimization of material properties [40-41]. In general, the experimental groups usually depend on the indirect support by transmission electron microscopy (TEM) or scanning tunneling microscopy (STM), in which the mistaken identification of defects are possible. Thus, the strong reliance on the STM image contrast of the atomic lattice and the weak difference between the chalcogen and metal sublattices has resulted in a non-consistent interpretation of the defect [42]. To overcome such a challenge, the demonstration of the influence of defect in charge couplings is highly required as the reference toolbox for the experimental scientists (**Figure 1**). Therefore, in this work, we have presented a comprehensive theoretical simulation of the defect-correlated STM images to reveal the self-activated charge coupling within the mono-layered α-In_2Se_3. Beyond the typical limited horizon supplied by the STM results, we utilize the density functional theory to illustrate both in-plane and out-of-plane charge disturbance within the defective structure. For the first time, our work has supplied a complete theoretical study of the charge distribution dominated by the major intrinsic defects regarding the simulated STM results and electronic structures, which significantly contributes as a guideline for future experimental scientists to understand the lattice structure and properties from an in-depth perspective.

Results and Discussion

Due to the synthesis challenge, the precise corresponding structural identification or the atomic arrangements are mostly concentrated on the bulk structures rather than the mono or few-layered α-In_2Se_3, which further limits the understanding of the origins of ferroelectricity and other unique properties. The phonon related lattice vibration is able to causes unique property alternation, which has rarely been discussed in LMC materials before. To connect our theoretical work with the experimental characterizations in a more comprehensive approach, we apply the mono-layered α-In_2Se_3 as our initial model to study the fundamental electronic structure and phonon dispersion (**Figure 2a**). Especially for the atomic-level thin film, the layer dependence induced the charge disturbance, which inevitably leads to the abnormal phonon dispersion shift, representing the distinct electronic behaviors. With the three-fold symmetry, the top Se and bottom Se positions overlap from the top view (**Figure 2b**). However, their valence charge densities are not correspondingly matched. Instead, we observe the shifting of charge density, indicating the inequivalent charge distribution within the lattice. To further look into the electronic structure, we also demonstrate the valence charge density distribution from the side view (**Figure 2c-2d**). Notably, the evident difference of the charge density features is noted, in which the top Se atom layer and the bottom Se atom layer display the s-like orbitals and the p-π orbitals, respectively. This further confirms the non-equivalent charge density in the mono-layered α-In_2Se_3, which supplied insightful information for the origins of ferroelectricity or piezoelectricity. To reveal the distinct lattice vibration in detail, we calculate the phonon dispersion of both mono-layered and multi-layered α-In_2Se_3 (**Figure 2e**). The optical branch and the acoustic branch have a scale of around 150 cm^{-1} and 100 cm^{-1}, respectively. Notably, there are kinks in both optical branches and acoustic branches near the highly symmetric gamma point. For the kinks in the optical branches, the scales of in mono-layered and multi-layered α-In_2Se_3 are similar (**Figure 2f**). However, the kink in the mono-layered has shifted towards the smaller wavevector at a lower frequency. In contrast, the kinks in the acoustic branches of both mono-layered and multi-layered α-In_2Se_3 locate at a close frequency with a similar scale. The same direction of kink shifting is also observed (**Figure 2g**). These unique phonon dispersion behaviors indicate the existence of Kohn anomalies in the ultra-thin α-In_2Se_3, which potentially induces the ferroelectric properties by the disturbed electron-phonon coupling [43]. In addition, by plotting the temperature dependence of frequency, a series of minor kinks from 25 K to 450 K including a dominant kink at 175 K can be clearly observed, indicating the sensitivity of lattice vibration to the temperature (**Figure 2h**). This correlates to the reversible phase change under thermal environment control [31]. Further analysis based on the first-order and second-order derivate of the temperature dependence of frequency also proved the high-temperature sensitivity (**Figure 2i-2j**). In particular, the strong kinks at 25 K and 320 K supports the existence of electron-phonon coupling behaviors in the mono-layered pristine α-In_2Se_3, which correlates to the room-temperature ferroelectricity of ultrathin α-In_2Se_3. The phonon dispersions not only show the potential Kohn anomalies induced discontinuity in the structure but also the layer-dependent phonon shifting. These strong electron-phonon couplings endow mono-layered α-In_2Se_3 potential of unique electronic structures [44].

Besides the fundamental lattice vibration, the detailed structural identification is also essential. Previous works have confirmed the increased instability of structure in the low dimensional materials, which leads to the pivotal role of defects in affecting the electronic behaviors [22, 44]. However, the detailed characterization of defects in In_2Se_3 is still very limited owing the synthesis difficulties and characterization challenges. Thus, we simulate the STM results of pristine α-In_2Se_3 with the structural difference to illustrate the charge couplings behaviors in mono-layered α-In_2Se_3. Notably, the pristine mono-layered α-In_2Se_3 structure has shown the absence of any contrast region, which is consistent with the feature of perfect lattice structure with even charge distribution (**Figure 3a-3d**). As part of the lattice structure shifts downwards, the structural change is immediately revealed by the simulated STM results. In different bias voltage, the downshifting feature unit is clearly noted. The evident triangle region with weak contrast directly corresponds to the three surface Se atoms at a lower level due to the downshifting. Meanwhile, the upshifting structure of α-In_2Se_3 displays the converse contrast of the simulated STM results. The upshifted Se triangle unit and centered In are reflected by the strong contrast region under the bias voltage of 2.0 V (**Figure 3e**). For simulated STM results under both 0.5 and -3.0 V bias voltage, the strong contrast triangle is still obvious to verify the upshifted lattice feature (**Figure 3f-3g**). The simulated STM results through deeper scanning are shown in **Figure S1**. These results indicate the significance of the theoretical calculations in revealing the microscopic structural changes.

How to accurately locate and identify the defects from structural characterizations is a remaining challenge, which requires the assistance of high-precision theoretical calculations. Firstly, the STM simulation in α-In_2Se_3 with the Se-vacancy (V_{Se}) has been performed under original, upshifting and downshifting situations with the bias voltage 2.0 V, 0.5 V and -3.0 V, respectively (**Figure 4a**). For the original V_{Se} model, the simulated STM images show a similar contrast at 2.0 V and 0.5 V bias voltages (**Figure 4b-4c**). Especially at 0.5 V bias voltage, the V_{Se} site forms an evident triangle area, indicating the electron fluctuation (**Figure 4d**). In comparison, the upshifting defective models show more contrast in the vacancy area (**Figure 4e**). For 2.0 V bias voltage, three levels of contrast are seen near the upshifting area, confirming the convex structure (**Figure 4f-4g**). This result is consistent with previous research on the anion vacancy in another LMC material Bi_2Se_3 [45]. However, under negative bias voltage, the detection of V_{Se} cannot be reflected by the STM results obtained by the deeper scanning tip distance, in which the contrast induced by the defect is neglectable (**Figure S2**). The contrast becomes much stronger when the bias voltage reduces to 0.5 V. The simulated STM image at -3.0 V bias voltage displays opposite contrast with the STM image at 2.0 V, which compensates as experimental characterization results (**Figure 4h**). In addition, the parallel line pattern along the three-fold symmetry directions, representing the long-range p-p directional coupling between atoms. Meanwhile, the simulated STM image of the downshifting defective model also reveals evident structural features by the electron fluctuation contrast, especially obvious for the downshifting structure under 2.0 V bias voltage (**Figure 4i-4j**). At 0.5 bias voltage, three levels of contrast within the well-ordered alignment of surrounding atoms are shown, supporting the gradual change of charge difference (**Figure 4k**). As the bias voltage reduces to -3.0 V, the contrast becomes lower that only two different levels of contrast are observed (**Figure 4l**). At the deeper scanning distance, V_{Se} sites are observed in different bias voltages with lower contrast (**Figure S2**).

Besides the most common anion vacancy defects, the critical cation In-vacancy (V_{In}) is studied through the simulated STM image for the first time to compare the induced structural difference (**Figure 5a**). The defect inevitably perturbs the electronic states predominantly along the In-Se ppσ chains, resulting in the three spots at surface atoms terminating the chains. Thus, the center joining the three spots is the lateral position of the defect. Under 2.0 V, the simulated STM image shows an evident contrast surround the V_{In} site (**Figure 5b**). When the bias voltage decreases to 0.5 V, the contrast of V_{In} site forms a bright triangle region [46]. Three different levels of contrasts are noticed near V_{In} site. Meanwhile, we also observe the well-ordered atom arrangements in the low contrast area (**Figure 5c**). When the bias voltage changes to -3.0 V, the simulated STM image displays a converse contrast with the result under 2.0 V, following the same atomic arrangements (**Figure 5d**). For scanning tip contacting the mid-layer of In_2Se_3, a similar contrast near V_{In} is confirmed (**Figure S3**). In contrast, the downshifting defective model exhibits the distinct simulated STM image patterns from the previous two models (**Figure 5e**). At 2.0 V bias voltage, the absence of contrast near V_{In} site is noticed. As the bias voltage becomes 0.5 V, the contrast appears as bright points in the large defective region (**Figure 5f-5g**). The simulated STM image under -3.0 V bias voltage is compensated with the pattern under positive bias voltage (**Figure 5h**). The strong contrast of the downshift area and the well-aligned stripes throughout the surface are observed. The STM images of -3.0 V with the deeper scanning distance also support that the converse results with the previous models under the bias voltage of 2.0 V and 0.5 V **(Figure S3)**. We further modify the lattice structure based on defective In_2Se_3 with V_{In} by upshifting the nearest Se atoms along the z-axis (**Figure 5i**). At the bias voltage of 2.0 V, the evident contrast is observed at the V_{In} site. However, the triangle feature of the vacancy becomes weaker (**Figure 5j**). The evident p-p orbital couplings of surface Se atoms are noted near the V_{In} model at 0.5 V bias voltage (**Figure 5k**). Moreover, the simulated STM image shows strong contrast at the -3.0 V, in which the V_{In} site is reflected by the blue triangle area as shown in **Figure 5l**. The STM images with a deeper tip scanning distance result in a similar pattern under different bias voltages (**Figure S3**).

Besides the commonly discussed vacancies defects in the lattice, the studies of other intrinsic defects in mono-layered α-In_2Se_3 including vacancy cluster, adatom and antisite are also highly desired to supply a comprehensive map as references for the experimental results. More importantly, such simulated STM image mapping of the detailed defective structures is demonstrated. For simulated STM image of In_2Se_3 with three V_{Se} defect clusters ($3V_{Se}$) on the surface, we notice the contrast between bright background with dark triangle area at the bias voltage of 2.0 V (**Figure 6a**). As the bias voltage reduces to 0.5 V, the contrast becomes stronger, in which the $3V_{Se}$ induced tringle bright part is clearly shown, indicating the strong charge coupling near the defect region. Moreover, several gradually changed levels of contrast in -3.0 V within the triangle area further confirm the existence $3V_{Se}$ on the surface during scanning. On the contrary, the defective model with surface Se_{ad} clearly demonstrates the top Se atoms on the surface (**Figure 6b**). Compared to the model with $3V_{Se}$ on the surface, we notice a smaller contrast region also concentrated near the adatom. Distinctly, the simulated STM image of In_{ad} reveals the triangle region including the top In-adatom and the coupling with the three neighboring Se atoms. We notice the contrast levels at the bias voltage of 0.5 V. Meanwhile, the contrast in 2.0 bias voltage and -3.0 bias voltage are completely opposite (**Figure 6c**). The anti-site defect is another common defect, in which the anion and cation atoms switch their positions during the synthesis approach or external excitation such as lattice vibration (**Figure 6d**). For the anti-site defect on the surface of α-In_2Se_3, the strong contrast area shows the uneven charge distribution near the defect, which is induced by the switch between Se and In atoms. More importantly, the formation of the evident contrast line and region indicates the potential possibility of the phase change, supporting the previous experimental reports [46]. The simulated results of In adatom defect and anti-site defect match the experimental results of surface defects in another LMC material Bi_2Te_3 with similar lattice structure [41]. Besides the consideration of the sublayer V_{Se}, the simulated STM images affected by the surface V_{Se} are also demonstrated (**Figure 6e**). At 0.5 V bias voltage, the simulated STM image shows an evident contrast within the hexagonal region. Under -2.0 V and 2.0 V, the simulated STM image shows a compensated pattern. In the end, we also reproduce the possible surface distortion structure, which originates from the surface vacancies induced surface instability (**Figure 6f**).

To further reflect the induced influence on the electronic structure by different defects, we demonstrate the projected partial density of states (PDOSs) of all the possible defective structures. As the range of the threshold in scanning tunneling spectroscopy (STS), we apply a similar concept to compare the defective structures regarding the gap between the dominant peak in the conduction band (CB) and valence band (VB), respectively. For all the structures, we notice the dominant role of p-orbitals, especially for the VB. Meanwhile, the s-orbitals only contribute to the CB. Since the long-range and short-range competition is achieved by the p-p orbital couplings, we only focus on the p-orbitals in defective structures. In the pristine structure, we notice the threshold locating near E_V-0.5 eV (E_V= 0 eV), displaying a gap of 3.50 eV for the electron transfer (**Figure 7a**). With the formation of $3V_{Se}$ on the surface, the gap between the dominant peaks of both CB and VB has reduced to 3.30 eV, in which the Fermi level (E_F) has shifted towards the middle of the gap (**Figure 7b**). The gap between the dominant peaks of both CB and VB further decreases to 3.05 eV, with E_F still pins near the valence band maximum (VBM) (**Figure 7c**). The PDOS of anti-site defects and Se adatom defects exhibit highly similar PDOS results, in which the E_F is pinned in the middle of the gap with a size of 3.10 eV (**Figure 7d-7e**). The position of E_F slightly shifts towards the CB with 0.1 eV increases in the gap between the dominant peaks of both CB and VB (**Figure 7f**). Similar to the defective structure with $3V_{Se}$, the existence of surface V_{Se} induces a smaller gap of 3.20 eV, which demonstrates the dominant peaks of VB and CB at E_V-1.7 eV and E_V+1.5 eV, respectively (**Figure 7g**). For the vacancies in the sublayers, their PDOSs are similar to the pristine In_2Se_3 with an alleviated gap between the thresholds in both CB and VB (**Figure 7h and 7i**). With these comprehensive mapping of the electronic structures of defective In_2Se_3, future experiments are able to identify the potential structure information based on insightful guidelines in this work.

After the detailed discussion of the defective structure characterizations of mono-layer In_2Se_3, the formation of defects in the few-layers In_2Se_3 is also considered from the energetic perspectives. Taking the $3V_{Se}$ as an example, the formation on the surfaces is significantly preferable than in the sublayers (**Figure 8a**). As the layer thickness increases, the formation energy of surface $3V_{Se}$ remains similar while that of the sublayer $3V_{Se}$ doubled from two layers to four layers. The bandgap changes are also illustrated (**Figure 8b**). As the layer increases, the defective In_2Se_3 with surface $3V_{Se}$ shows the same trend of bandgap variation with the pristine In_2Se_3. However, the sublayer $3V_{Se}$ induces an opposite trend. In addition, the upshifting of the In_2Se_3 surface is noted under 2.0 V applied voltage, displaying a distance up to 0.6 nm induced by the surface vacancies (**Figure 8c**). Then, the total density of states (TDOS) is also shown to demonstrate the electronic structure difference induced by the layer changes. For the few-layered pristine In_2Se_3, the gap between the thresholds gradually decreases as the layer increases (**Figure 8d**). Moreover, the overall gap scale between CB and VB significantly shrinks when compared to the monolayer. Notably, the formation of surface $3V_{Se}$ modulates the electronic structures in terms of the band positions, especially to the thickness over 2 layers (**Figure 8e**), indicating the importance of surface $3V_{Se}$ to the electronic behaviors of ultra-thin In_2Se_3 films. The formation of surface $3V_{Se}$ substantially enlarges the gap size between CB and VB. On the other hand, the sublayer $3V_{Se}$ also shows a similar effect on the gap scale between CB and VB (**Figure 8f**). Nevertheless, the TDOSs of defective In_2Se_3 with sublayer $3V_{Se}$ still shows similar results with the pristine In_2Se_3, demonstrating the limited modulation by the sublayer defects. For all the models, the shifting of PDOS the multilayer In_2Se_3 is more evident as the layer thickness increases, which indicates the potential deviation of the symmetry center and the change of electronic structure. Notably, the existence of defects has significantly enlarged the PDOS shifting, indicating the perturbation of charge distribution of the structure, which further leads to the ferroelectricity of the atomic-layer In_2Se_3. Compared with the phonon dispersion (**Figure 2**), the similar shifting induced by the layer increases is also observed, which supports the change of the charge distribution. Besides the vacancy, the layer-dependence of the lattice dynamics illustrates a promising approach for the control and modulation of ferroelectricity or piezoelectricity in the ultra-thin 2D LMC materials.

Conclusion

In summary, this work has presented a full picture of major intrinsic defects in both the mono- and few-layered α-In_2Se_3 to demonstrate the general mechanism of the defects activated charge coupling behaviors. By detailed analysis of the simulated STM images and phonon behaviors under different defects, this work supplies the insightful structure clues of the nanoscale charge distribution fluctuations, explaining the unique electronic behaviors in mono-layered α-In_2Se_3. Furthermore, we confirm the high possibility of surface defects in the few-layered α-In_2Se_3 rather than sub-layered defects. The modulations of the electronic properties by different intrinsic defects regarding the charge couplings and bandgap have been revealed, which is of significance in the precise identification and modulation of the ultra-thin LMC based ferroelectric materials, shedding new light for the synthesis of other relevant functional materials for broad applications.

Acknowledgements

The authors gratefully acknowledge the support of the Natural Science Foundation of China (Grant No.: NSFC 21771156), and the Early Career Scheme (ECS) fund (Grant No.: PolyU 253026/16P) from the Research Grant Council (RGC) in Hong Kong.

Declaration of interest

The authors declare no competing interest.

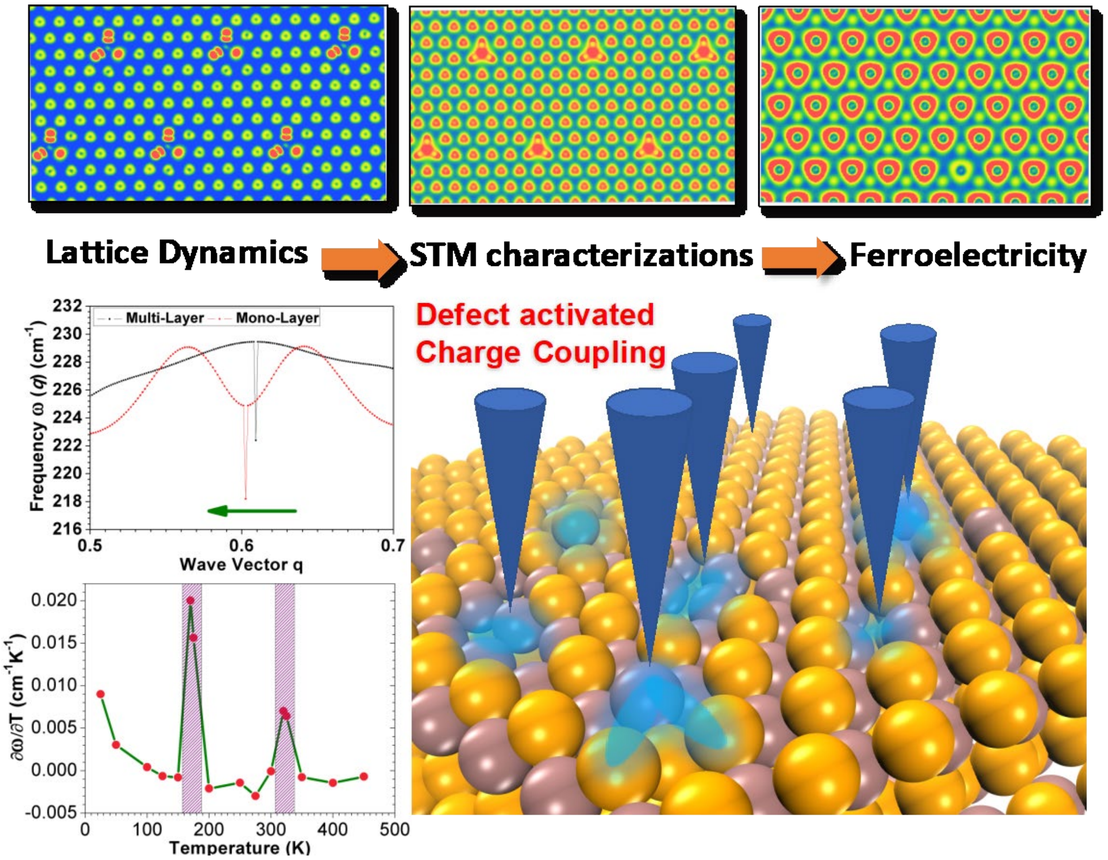

Figure 1. The illustration of major intrinsic defects identification and induced charge couplings in 2D layered metal chalcogenides.

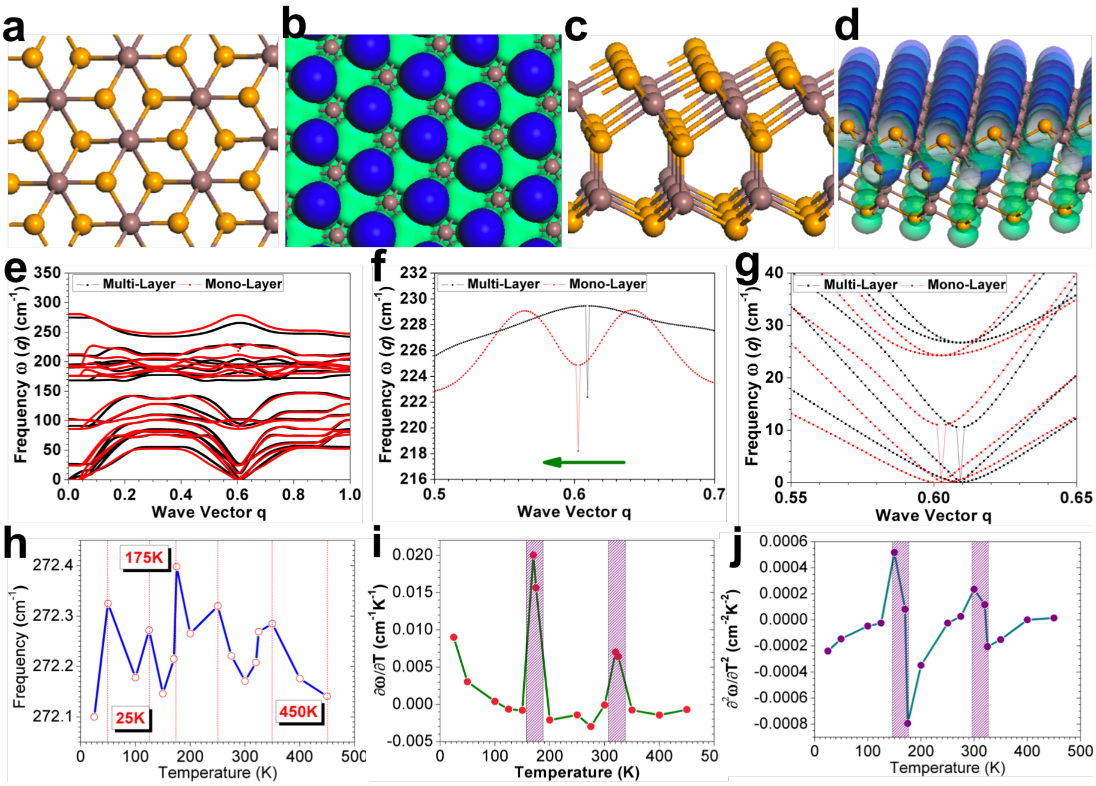

Figure 2. The electronic structure and phonon dispersion of In$_2$Se$_3$. (a) The top view of mono-layered α-In$_2$Se$_3$. (b) The valence charge density distribution from the top view. Blue isosurfaces represent the valence charge density of the top surface Se atom layer. Green isosurfaces represent the valence charge density of the bottom Se atom layer. (c) The side view of mono-layered α-In$_2$Se$_3$. (d) The valence charge density distribution from the side view. Blue isosurfaces represent the valence charge density of the top surface Se atom layer. (e) The phonon dispersion of mono-layered and multi-layered α-In$_2$Se$_3$. (f) The enlarged display of the kink in the optical branches of the phonon dispersion. (g) The enlarged display of the kink in the acoustic branches of the phonon dispersion. (h) The dependence of frequency at Gamma point on temperature from 25 K- 450 K. (i) The first-order derivative of frequency on temperature from 25 K to 450 K. (j) The second-order derivative of frequency on temperature from 25 K to 450 K.

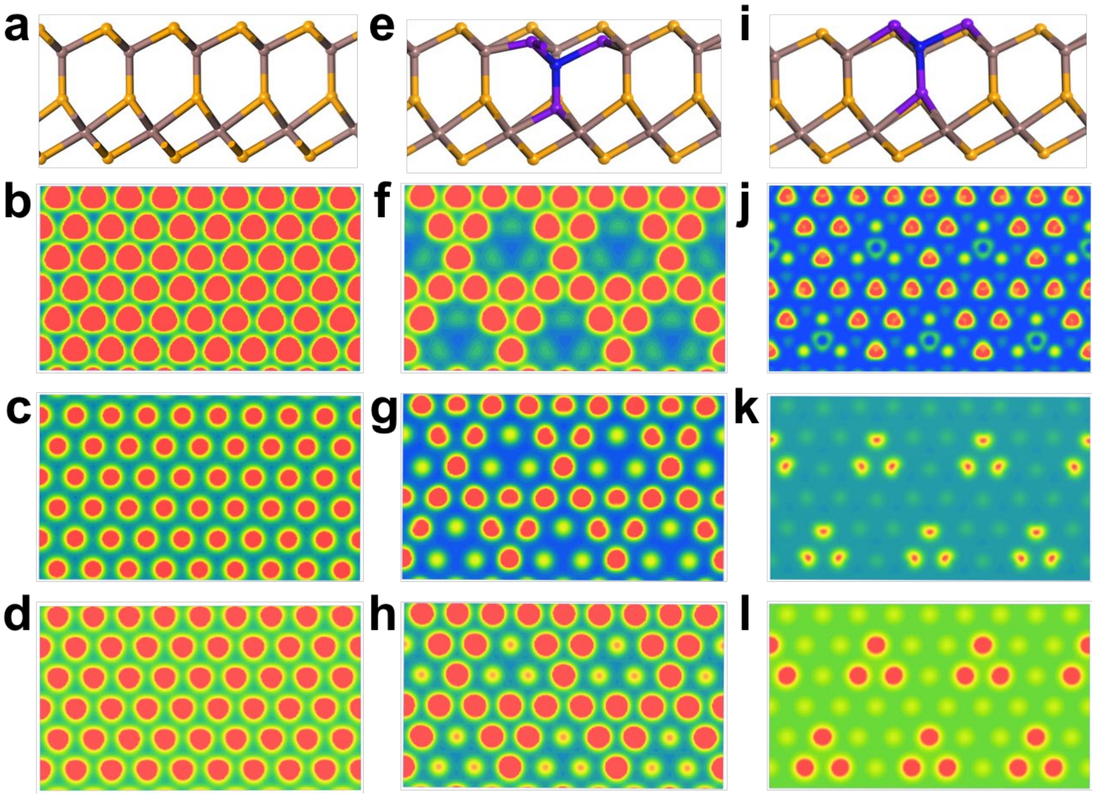

Figure 3. The STM images of the upshifting and downshifting structure of mono-layered α-In_2Se_3. **(a)** The structure of mono-layered α-In_2Se_3. The STM image of mono-layered α-In_2Se_3 under a bias voltage of **(b)** 2.0 V **(c)** 0.5 V and **(d)** -3.0 V. **(e)** The structure of mono-layered downshifting α-In_2Se_3. The purple balls and blue balls represent the shifting region. Purple ball = Se and blue ball = In. STM image of mono-layered downshifting α-In_2Se_3 under bias voltage of **(f)** 2.0 V **(g)** 0.5 V and **(h)** -3.0 V. **(i)** The structure of mono-layered upshifting α-In_2Se_3. The STM image of mono-layered α-In_2Se_3 under bias voltage of **(j)** 2.0 V **(k)** 0.5 V and **(l)** -3.0 V.

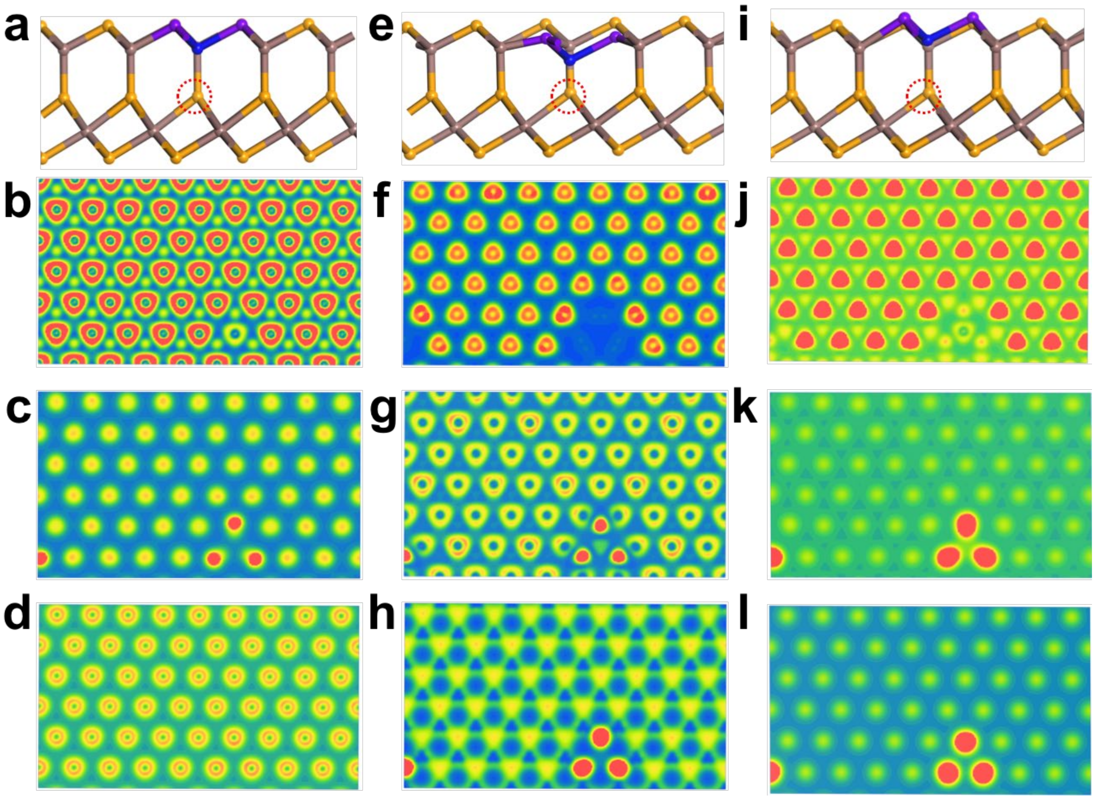

Figure 4. The STM images of the upshifting and downshifting structure of mono-layered α-In_2Se_3 with sublayer Se-vacancy. **(a)** The structure of mono-layered α-In_2Se_3 with sublayer Se-vacancy. The purple balls and blue balls represent the defective region. Purple ball = Se and blue ball = In. The red dash circle is the Se-vacancy. The STM image of mono-layered α-In_2Se_3 with sublayer Se-vacancy under a bias voltage of **(b)** 2.0 V **(c)** 0.5 V and **(d)** -3.0 V. **(e)** The structure of mono-layered downshifting α-In_2Se_3 with sublayer Se-vacancy. The STM image of mono-layered downshifting α-In_2Se_3 with sublayer Se-vacancy under a bias voltage of **(f)** 2.0 V **(g)** 0.5 V and **(h)** -3.0 V. **(i)** The structure of mono-layered upshifting α-In_2Se_3 with sublayer Se-vacancy. The STM image of mono-layered α-In_2Se_3 with sublayer Se-vacancy under a bias voltage of **(j)** 2.0 V **(k)** 0.5 V and **(l)** -3.0 V.

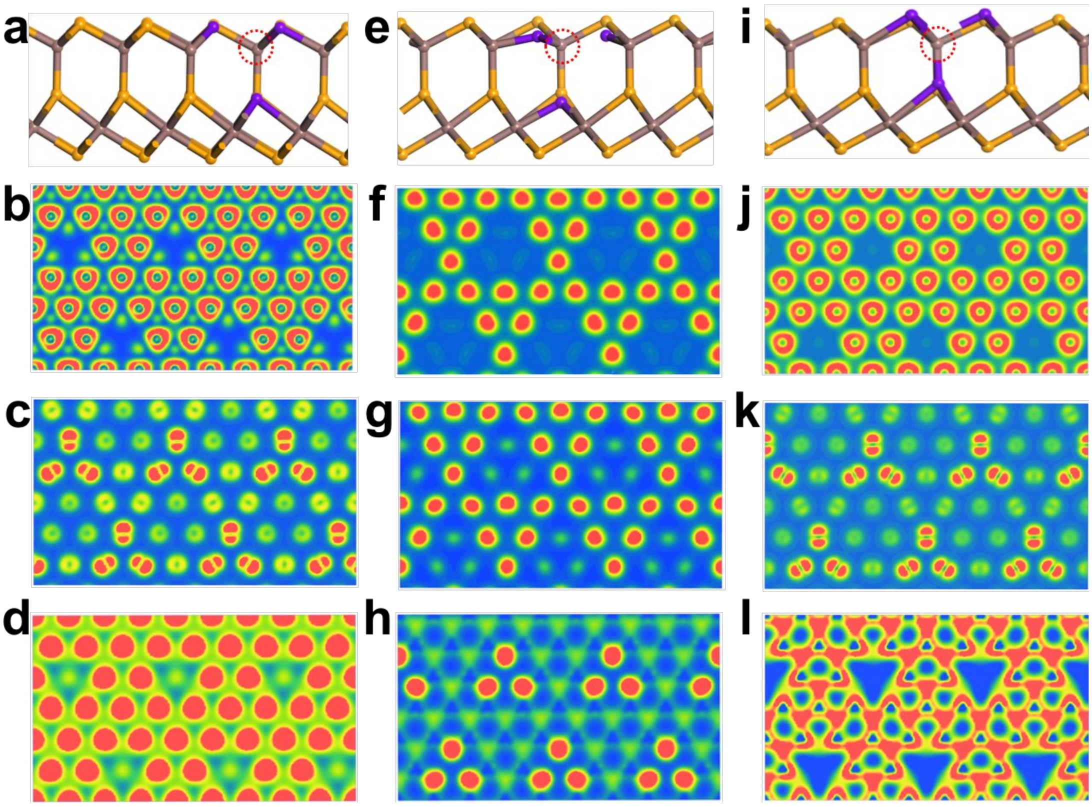

Figure 5. The STM images of the upshifting and downshifting structure of mono-layered α-In$_2$Se$_3$ with sublayer In-vacancy. **(a)** The structure of mono-layered α-In$_2$Se$_3$ with sublayer In-vacancy. The purple balls and blue balls represent the defective region. Purple ball = Se and blue ball = In. The red dash circle is the In-vacancy. The STM image of mono-layered α-In$_2$Se$_3$ with sublayer In-vacancy under a bias voltage of **(b)** 2.0 V **(c)** 0.5 V and **(d)** -3.0 V. **(e)** The structure of mono-layered downshifting α-In$_2$Se$_3$ with sublayer In-vacancy. The STM image of mono-layered downshifting α-In$_2$Se$_3$ with sublayer In-vacancy under a bias voltage of **(f)** 2.0 V **(g)** 0.5 V and **(h)** -3.p V. **(i)** The structure of mono-layered upshifting α-In$_2$Se$_3$ with sublayer Se-vacancy. The STM image of mono-layered α-In$_2$Se$_3$ with sublayer In-vacancy under a bias voltage of **(j)** 2.0 V **(k)** 0.5 V and **(l)** -3.0 V.

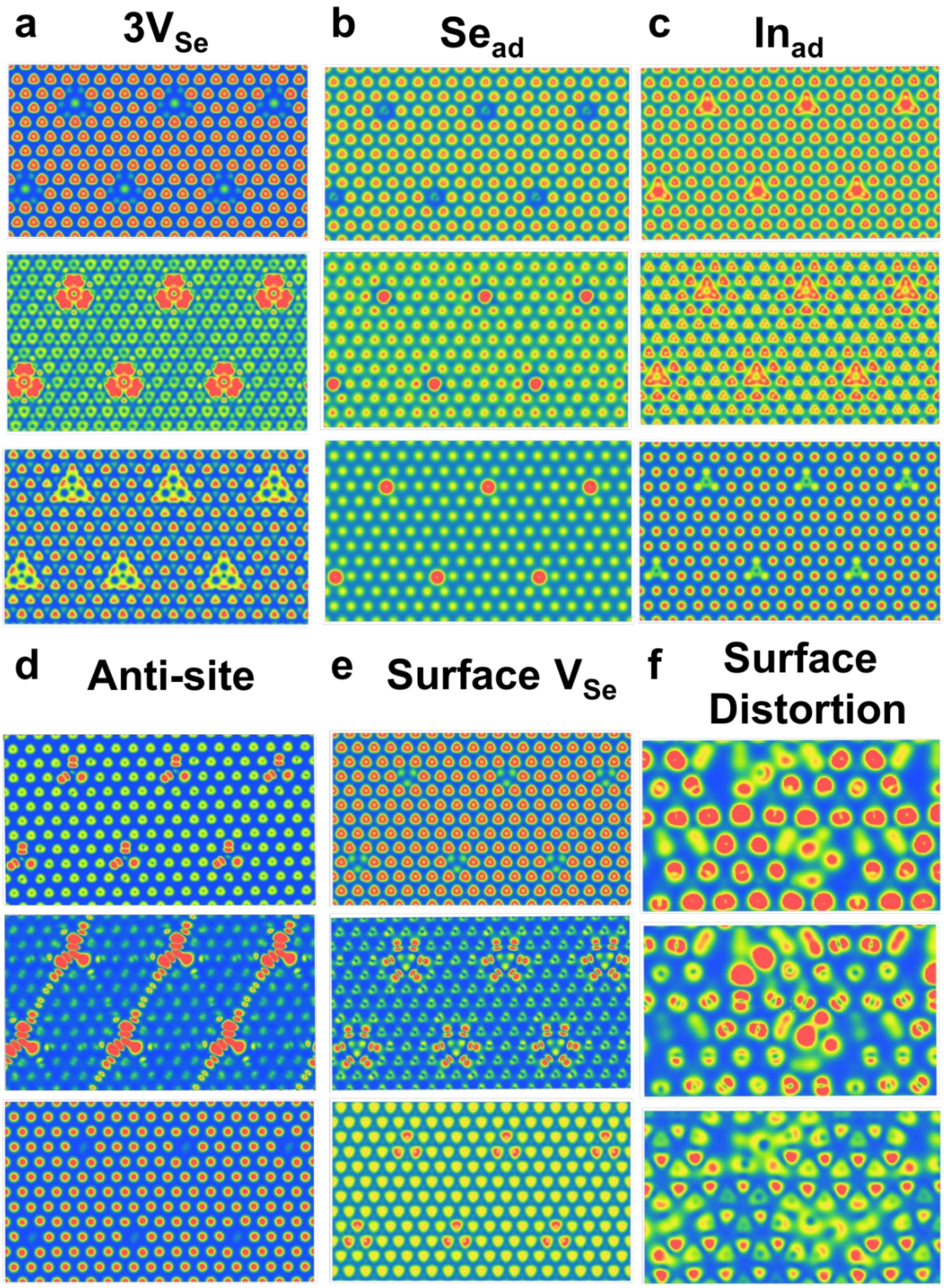

Figure 6. The STM images of mono-layered α-In_2Se_3 with different intrinsic defects. **(a)** The structure of mono-layered α-In_2Se_3 with surface 3 Se-vacancy cluster under bias voltage of 2.0 V, 0.5 V and -3.0 V. **(b)** The structure of mono-layered α-In_2Se_3 with surface Se ad-atom under bias voltage of 2.0 V, 0.5 V and -3.0 V. **(c)** The structure of mono-layered α-In_2Se_3 with surface In ad-atom under bias voltage of 2.0 V, 0.5 V and -3.0 V. **(d)** The structure of mono-layered α-In_2Se_3 with surface Se-vacancy cluster under bias voltage of 2.0 V, 0.5 V and -3.0 V. **(e)** The structure of mono-layered α-In_2Se_3 with anti-site defect under bias voltage of 2.0 V, 0.5 V and -3.0 V. **(f)** The structure of mono-layered α-In_2Se_3 with surface reconstruction under bias voltage of 2.0 V, 0.5 V, and -3.0 V.

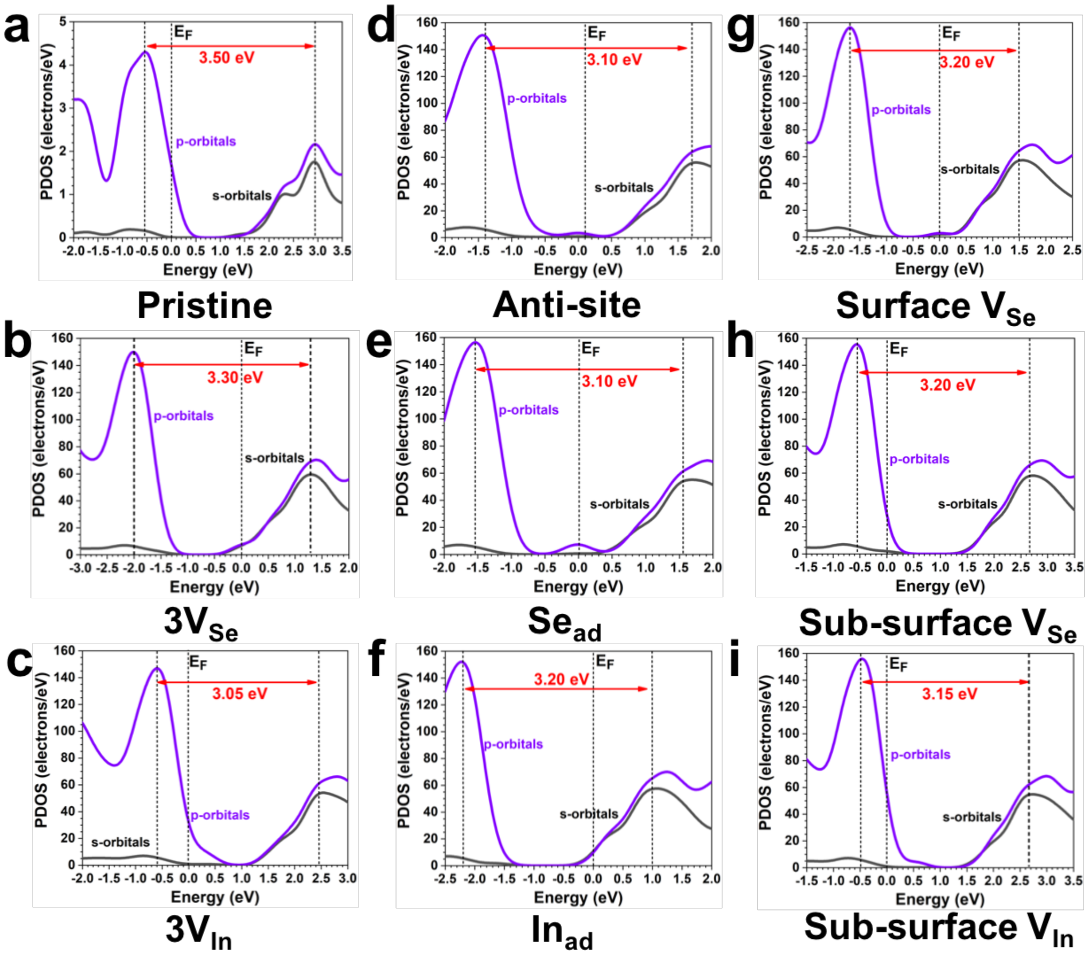

Figure 7. The PDOS of mono-layered α-In_2Se_3 with different intrinsic defects. (a) Pristine. **(b)** With $3V_{Se}$ on the surface. **(c)** With $3V_{In}$. **(d)** With antisite defect. **(e)** With Se adatom. **(f)** With In adatom. **(g)** With surface V_{Se}. **(h)** With sub-surface V_{Se}. **(i)** With sub-surface V_{In}.

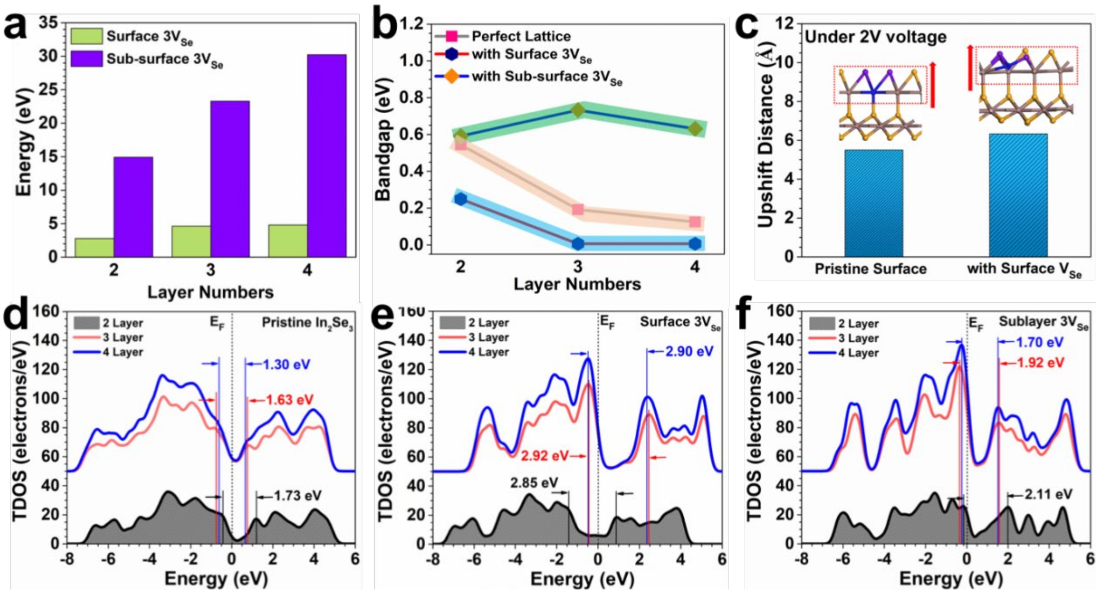

Figure 8. The energetic and electronic investigation of few-layered α-In$_2$Se$_3$. (a) The formation energies of surface 3V$_{Se}$ and sub-surface 3V$_{Se}$. **(b)** The bandgap changes in surface 3V$_{Se}$ and sub-surface 3V$_{Se}$. **(c)** The upshifting distance comparison for pristine and defective α-In$_2$Se$_3$ under a bias voltage of 2.0 V. (**d**) The TDOS of few-layered α-In$_2$Se$_3$. **(e)** The TDOS of few-layered α-In$_2$Se$_3$ with surface 3V$_{Se}$. **(f)** The TDOS of few-layered α-In$_2$Se$_3$ with sub-surface 3V$_{Se}$.

Reference:

[1] D. Akinwande; C. Huyghebaert; C.-H. Wang; M. I. Serna; S. Goossens; L.-J. Li; H. S. P. Wong; F. H. L. Koppens, Graphene and Two-Dimensional Materials for Silicon Technology. *Nature* **2019,** *573* (7775), 507-518.

[2] G. R. Bhimanapati; Z. Lin; V. Meunier; Y. Jung; J. Cha; S. Das; D. Xiao; Y. Son; M. S. Strano; V. R. Cooper; L. Liang; S. G. Louie; E. Ringe; W. Zhou; S. S. Kim; R. R. Naik; B. G. Sumpter; H. Terrones; F. Xia; Y. Wang; J. Zhu; D. Akinwande; N. Alem; J. A. Schuller; R. E. Schaak; M. Terrones; J. A. Robinson, Recent Advances in Two-Dimensional Materials Beyond Graphene. *ACS Nano* **2015,** *9* (12), 11509-11539.

[3] W. Wu; L. Wang; Y. Li; F. Zhang; L. Lin; S. Niu; D. Chenet; X. Zhang; Y. Hao; T. F. Heinz; J. Hone; Z. L. Wang, Piezoelectricity of Single-Atomic-Layer Mos2 for Energy Conversion and Piezotronics. *Nature* **2014,** *514* (7523), 470-4.

[4] M. Chhowalla; H. S. Shin; G. Eda; L.-J. Li; K. P. Loh; H. Zhang, The Chemistry of Two-Dimensional Layered Transition Metal Dichalcogenide Nanosheets. *Nature Chemistry* **2013,** *5* (4), 263-275.

[5] J. N. Coleman; M. Lotya; A. O'Neill; S. D. Bergin; P. J. King; U. Khan; K. Young; A. Gaucher; S. De; R. J. Smith; I. V. Shvets; S. K. Arora; G. Stanton; H. Y. Kim; K. Lee; G. T. Kim; G. S. Duesberg; T. Hallam; J. J. Boland; J. J. Wang; J. F. Donegan; J. C. Grunlan; G. Moriarty; A. Shmeliov; R. J. Nicholls; J. M. Perkins; E. M. Grieveson; K. Theuwissen; D. W. McComb; P. D. Nellist; V. Nicolosi, Two-Dimensional Nanosheets Produced by Liquid Exfoliation of Layered Materials. *Science* **2011,** *331* (6017), 568-571.

[6] X. Qian; J. Liu; L. Fu; J. Li, Quantum Spin Hall Effect in Two-Dimensional Transition Metal Dichalcogenides. *Science* **2014,** *346* (6215), 1344-1347.

[7] K. Tran; G. Moody; F. Wu; X. Lu; J. Choi; K. Kim; A. Rai; D. A. Sanchez; J. Quan; A. Singh; J. Embley; A. Zepeda; M. Campbell; T. Autry; T. Taniguchi; K. Watanabe; N. Lu; S. K. Banerjee; K. L. Silverman; S. Kim; E. Tutuc; L. Yang; A. H. MacDonald; X. Li, Evidence for Moiré Excitons in Van Der Waals Heterostructures. *Nature* **2019,** *567* (7746), 71-75.

[8] C. Huang; S. Wu; A. M. Sanchez; J. J. P. Peters; R. Beanland; J. S. Ross; P. Rivera; W. Yao; D. H. Cobden; X. Xu, Lateral Heterojunctions within Monolayer Mose2–Wse2 Semiconductors. *Nature Materials* **2014,** *13* (12), 1096-1101.

[9] C. Tan; Z. Lai; H. Zhang, Ultrathin Two-Dimensional Multinary Layered Metal

Chalcogenide Nanomaterials. *Adv Mater* **2017,** *29* (37), 1701392.

[10] A. K. Geim; I. V. Grigorieva, Van Der Waals Heterostructures. *Nature* **2013,** *499* (7459), 419-425.

[11] R. B. Jacobs-Gedrim; M. Shanmugam; N. Jain; C. A. Durcan; M. T. Murphy; T. M. Murray; R. J. Matyi; R. L. Moore, 2nd; B. Yu, Extraordinary Photoresponse in Two-Dimensional in(2)Se(3) Nanosheets. *ACS Nano* **2014,** *8* (1), 514-21.

[12] C. Qiu; B. Wang; N. Zhang; S. Zhang; J. Liu; D. Walker; Y. Wang; H. Tian; T. R. Shrout; Z. Xu; L. Q. Chen; F. Li, Transparent Ferroelectric Crystals with Ultrahigh Piezoelectricity. *Nature* **2020,** *577* (7790), 350-354.

[13] Y. Nahas; S. Prokhorenko; J. Fischer; B. Xu; C. Carretero; S. Prosandeev; M. Bibes; S. Fusil; B. Dkhil; V. Garcia; L. Bellaiche, Inverse Transition of Labyrinthine Domain Patterns in Ferroelectric Thin Films. *Nature* **2020,** *577* (7788), 47-51.

[14] Y. M. You; W. Q. Liao; D. Zhao; H. Y. Ye; Y. Zhang; Q. Zhou; X. Niu; J. Wang; P. F. Li; D. W. Fu; Z. Wang; S. Gao; K. Yang; J. M. Liu; J. Li; Y. Yan; R. G. Xiong, An Organic-Inorganic Perovskite Ferroelectric with Large Piezoelectric Response. *Science* **2017,** *357* (6348), 306-309.

[15] B. Radisavljevic; A. Radenovic; J. Brivio; V. Giacometti; A. Kis, Single-Layer Mos2 Transistors. *Nat Nanotechnol* **2011,** *6* (3), 147-50.

[16] G. Gao; J. Yu; X. Yang; Y. Pang; J. Zhao; C. Pan; Q. Sun; Z. L. Wang, Triboiontronic Transistor of Mos2. *Adv Mater* **2019,** *31* (7), e1806905.

[17] C. Wu; T. W. Kim; J. H. Park; H. An; J. Shao; X. Chen; Z. L. Wang, Enhanced Triboelectric Nanogenerators Based on Mos2 Monolayer Nanocomposites Acting as Electron-Acceptor Layers. *ACS Nano* **2017,** *11* (8), 8356-8363.

[18] J. Zhao; Z. Wei; Q. Zhang; H. Yu; S. Wang; X. Yang; G. Gao; S. Qin; G. Zhang; Q. Sun; Z. L. Wang, Static and Dynamic Piezopotential Modulation in Piezo-Electret Gated Mos2 Field-Effect Transistor. *ACS Nano* **2019,** *13* (1), 582-590.

[19] W. Choi; N. Choudhary; G. H. Han; J. Park; D. Akinwande; Y. H. Lee, Recent Development of Two-Dimensional Transition Metal Dichalcogenides and Their Applications. *Mater Today* **2017,** *20* (3), 116-130.

[20] Y. Lai; Z. Song; Y. Wan; M. Xue; C. Wang; Y. Ye; L. Dai; Z. Zhang; W. Yang; H. Du; J. Yang, Two-Dimensional Ferromagnetism and Driven Ferroelectricity in Van Der Waals Cucrp2s6. *Nanoscale* **2019,** *11* (12), 5163-5170.

[21] L. You; Y. Zhang; S. Zhou; A. Chaturvedi; S. A. Morris; F. Liu; L. Chang; D.

Ichinose; H. Funakubo; W. Hu; T. Wu; Z. Liu; S. Dong; J. Wang, Origin of Giant Negative Piezoelectricity in a Layered Van Der Waals Ferroelectric. *Sci Adv* **2019,** *5* (4), eaav3780.

[22] J. Junquera; P. Ghosez, Critical Thickness for Ferroelectricity in Perovskite Ultrathin Films. *Nature* **2003,** *422* (6931), 506-9.

[23] J. J. Wang; F. F. Cao; L. Jiang; Y. G. Guo; W. P. Hu; L. J. Wan, High Performance Photodetectors of Individual Inse Single Crystalline Nanowire. *J Am Chem Soc* **2009,** *131* (43), 15602-3.

[24] T. Zhai; X. Fang; M. Liao; X. Xu; L. Li; B. Liu; Y. Koide; Y. Ma; J. Yao; Y. Bando; D. Golberg, Fabrication of High-Quality In2se3 Nanowire Arrays toward High-Performance Visible-Light Photodetectors. *ACS Nano* **2010,** *4* (3), 1596-1602.

[25] L. Heon; K. Young Keun; K. Donghwan; K. Dae-Hwan, Switching Behavior of Indium Selenide-Based Phase-Change Memory Cell. *IEEE Transactions on Magnetics* **2005,** *41* (2), 1034-1036.

[26] Hailin Peng; Xiao Feng Zhang; Ray D. Twesten; Y. Cui, Vacancy Ordering and Lithium Insertion in Iii2vi3 Nanowires *Nano Research* **2009,** *2*, 327-335.

[27] X. Tao; Y. Gu, Crystalline-Crystalline Phase Transformation in Two-Dimensional In2se3 Thin Layers. *Nano Lett* **2013,** *13* (8), 3501-5.

[28] H. Peng; D. T. Schoen; S. Meister; X. F. Zhang; Y. Cui, Synthesis and Phase Transformation of In2se3and Cuinse2nanowires. *J Am Chem Soc* **2007,** *129* (1), 34-35.

[29] W. Feng; W. Zheng; F. Gao; X. Chen; G. Liu; T. Hasan; W. Cao; P. Hu, Sensitive Electronic-Skin Strain Sensor Array Based on the Patterned Two-Dimensional A-In2se3. *Chem Mater* **2016,** *28* (12), 4278-4283.

[30] F. Xue; J. Zhang; W. Hu; W.-T. Hsu; A. Han; S.-F. Leung; J.-K. Huang; Y. Wan; S. Liu; J. Zhang; J.-H. He; W.-H. Chang; Z. L. Wang; X. Zhang; L.-J. Li, Multidirection Piezoelectricity in Mono- and Multilayered Hexagonal A-In2se3. *ACS Nano* **2018,** *12* (5), 4976-4983.

[31] F. Zhang; Z. Wang; J. Dong; A. Nie; J. Xiang; W. Zhu; Z. Liu; C. Tao, Atomic-Scale Observation of Reversible Thermally Driven Phase Transformation in 2d In2se3. *ACS Nano* **2019,** *13* (7), 8004-8011.

[32] W. Ding; J. Zhu; Z. Wang; Y. Gao; D. Xiao; Y. Gu; Z. Zhang; W. Zhu, Prediction of Intrinsic Two-Dimensional Ferroelectrics in In2se3 and Other Iii2-Vi3 Van Der Waals Materials. *Nat Commun* **2017,** *8*, 14956.

[33] Y. Zhou; D. Wu; Y. Zhu; Y. Cho; Q. He; X. Yang; K. Herrera; Z. Chu; Y. Han; M. C. Downer; H. Peng; K. Lai, Out-of-Plane Piezoelectricity and Ferroelectricity in Layered Alpha-In2se3 Nanoflakes. *Nano Lett* **2017,** *17* (9), 5508-5513.

[34] C. Zheng; L. Yu; L. Zhu; J. L. Collins; D. Kim; Y. Lou; C. Xu; M. Li; Z. Wei; Y. Zhang; M. T. Edmonds; S. Li; J. Seidel; Y. Zhu; J. Z. Liu; W. X. Tang; M. S. Fuhrer, Room Temperature in-Plane Ferroelectricity in Van Der Waals In2se3. *Sci Adv* **2018,** *4* (7), eaar7720.

[35] C. Cui; W.-J. Hu; X. Yan; C. Addiego; W. Gao; Y. Wang; Z. Wang; L. Li; Y. Cheng; P. Li; X. Zhang; H. N. Alshareef; T. Wu; W. Zhu; X. Pan; L.-J. Li, Intercorrelated in-Plane and out-of-Plane Ferroelectricity in Ultrathin Two-Dimensional Layered Semiconductor In2se3. *Nano Lett* **2018,** *18* (2), 1253-1258.

[36] Q. L. Li; Y. Li; J. Gao; S. D. Wang; X. H. Sun, High Performance Single In2se3 Nanowire Photodetector. *Appl Phys Lett* **2011,** *99* (24), 243105.

[37] J. Zhou; Q. Zeng; D. Lv; L. Sun; L. Niu; W. Fu; F. Liu; Z. Shen; C. Jin; Z. Liu, Controlled Synthesis of High-Quality Monolayered Alpha-In2se3 Via Physical Vapor Deposition. *Nano Lett* **2015,** *15* (10), 6400-5.

[38] Y. Hu; W. Feng; M. Dai; H. Yang; X. Chen; G. Liu; S. Zhang; P. Hu, Temperature-Dependent Growth of Few Layer B-Inse and A-In2se3 Single Crystals for Optoelectronic Device. *Semicond Sci Technol* **2018,** *33* (12), 125002.

[39] D. Wu; A. J. Pak; Y. Liu; Y. Zhou; X. Wu; Y. Zhu; M. Lin; Y. Han; Y. Ren; H. Peng; Y. H. Tsai; G. S. Hwang; K. Lai, Thickness-Dependent Dielectric Constant of Few-Layer in(2)Se(3) Nanoflakes. *Nano Lett* **2015,** *15* (12), 8136-40.

[40] S. Chen; X. Zhang; J. Zhao; Y. Zhang; G. Kong; Q. Li; N. Li; Y. Yu; N. Xu; J. Zhang; K. Liu; Q. Zhao; J. Cao; J. Feng; X. Li; J. Qi; D. Yu; J. Li; P. Gao, Atomic Scale Insights into Structure Instability and Decomposition Pathway of Methylammonium Lead Iodide Perovskite. *Nat Commun* **2018,** *9* (1), 4807.

[41] S. Fiedler; L. El-Kareh; S. V. Eremeev; O. E. Tereshchenko; C. Seibel; P. Lutz; K. A. Kokh; E. V. Chulkov; T. V. Kuznetsova; V. I. Grebennikov; H. Bentmann; M. Bode; F. Reinert, Defect and Structural Imperfection Effects on the Electronic Properties of Bitei Surfaces. *New Journal of Physics* **2014,** *16* (7), 075013.

[42] H.-P. Komsa; S. Kurasch; O. Lehtinen; U. Kaiser; A. V. Krasheninnikov, From Point to Extended Defects in Two-Dimensional Mos2: Evolution of Atomic Structure under Electron Irradiation. *Physical Review B* **2013,** *88* (3).

[43] M. Sun; B. Huang, Phonon Evidence of Kohn Anomalies in Nanogenerator Zno. *Nano Energy* **2019,** *59*, 626-635.

[44] X. Wan; S. Y. Savrasov, Turning a Band Insulator into an Exotic Superconductor. *Nat Commun* **2014,** *5*, 4144.

[45] J. Dai; D. West; X. Wang; Y. Wang; D. Kwok; S. W. Cheong; S. B. Zhang; W. Wu, Toward the Intrinsic Limit of the Topological Insulator Bi_2Se_3. *Phys Rev Lett* **2016,** *117* (10), 106401.

[46] Y. Jiang; Y. Y. Sun; M. Chen; Y. Wang; Z. Li; C. Song; K. He; L. Wang; X. Chen; Q. K. Xue; X. Ma; S. B. Zhang, Fermi-Level Tuning of Epitaxial Sb2te3 Thin Films on Graphene by Regulating Intrinsic Defects and Substrate Transfer Doping. *Phys Rev Lett* **2012,** *108* (6), 066809.